

# Numerical simulations of the separated flow around a freight train passing through a tunnel using the sliding mesh technique

Iliadis, Panagiotis; Hemida, Hassan; Soper, David; Baker, Christopher

DOI:

[10.1177/0954409719851421](https://doi.org/10.1177/0954409719851421)

License:

None: All rights reserved

Document Version

Peer reviewed version

Citation for published version (Harvard):

Iliadis, P, Hemida, H, Soper, D & Baker, C 2019, 'Numerical simulations of the separated flow around a freight train passing through a tunnel using the sliding mesh technique', *Proceedings of the Institution of Mechanical Engineers, Part F: Journal of Rail and Rapid Transit*. <https://doi.org/10.1177/0954409719851421>

[Link to publication on Research at Birmingham portal](#)

## Publisher Rights Statement:

Checked for eligibility: 18/06/2019

Iliadis, P., Hemida, H., Soper, D., Baker, C., Numerical simulations of the separated flow around a freight train passing through a tunnel using the sliding mesh technique, *Proceedings of the Institution of Mechanical Engineers, Part F: Journal of Rail and Rapid Transit* Copyright © IMechE 2019. DOI: 10.1177/0954409719851421

## General rights

Unless a licence is specified above, all rights (including copyright and moral rights) in this document are retained by the authors and/or the copyright holders. The express permission of the copyright holder must be obtained for any use of this material other than for purposes permitted by law.

- Users may freely distribute the URL that is used to identify this publication.
- Users may download and/or print one copy of the publication from the University of Birmingham research portal for the purpose of private study or non-commercial research.
- User may use extracts from the document in line with the concept of 'fair dealing' under the Copyright, Designs and Patents Act 1988 (?)
- Users may not further distribute the material nor use it for the purposes of commercial gain.

Where a licence is displayed above, please note the terms and conditions of the licence govern your use of this document.

When citing, please reference the published version.

## Take down policy

While the University of Birmingham exercises care and attention in making items available there are rare occasions when an item has been uploaded in error or has been deemed to be commercially or otherwise sensitive.

If you believe that this is the case for this document, please contact [UBIRA@lists.bham.ac.uk](mailto:UBIRA@lists.bham.ac.uk) providing details and we will remove access to the work immediately and investigate.

Article type: Original research

Corresponding Author:

Panagiotis Iliadis, School of Engineering, University of Birmingham, Edgbaston, Birmingham, B15 2TT, UK

E-mail: [pxi563@bham.ac.uk](mailto:pxi563@bham.ac.uk)

## **Numerical simulations of the separated flow around a freight train passing through a tunnel using the sliding mesh technique**

**P. Iliadis\*, H. Hemida, D. Soper, C. Baker**

School of Engineering, University of Birmingham, Edgbaston, Birmingham, B15 2TT, UK

Corresponding author e-mail: [pxi563@bham.ac.uk](mailto:pxi563@bham.ac.uk)

### **ABSTRACT**

The main aim of this investigation is to analyse the flow around a freight train as it passes through a tunnel. The separated flow around the train nose is related to energy losses, lateral vibration, noise, streamline deviation and influences the velocity magnitudes around the train. Such effects are expected to become more important with the prospect of increasing freight train speeds. The numerical simulations performed in this study use a Class 66 locomotive connected to eight container wagons, scaled to  $1/25^{\text{th}}$ , moving at a train speed of 33.5m/s through a tunnel with a blockage ratio of 0.202. The k-omega model combined with a high advection scheme, solves the governing equations on a structured hexahedral mesh using the sliding mesh technique. The pressure histories at the tunnel walls and train surface as well as the velocity field around the train were validated with experimental data obtained using a moving model. The longest separation bubble is found at the middle-height and middle-width of the locomotive due to extended corners at these regions. When the train enters the tunnel, the separation length is reduced by 32% at the roof and 31% at the sides, compared to open air. The maximum separation length is found at the sides of the train where it reattaches at 19% of the locomotive length, influencing the velocity peak at a short distance from the train surface. The larger the

separation length, the higher the length/duration of this peak. When the train head is halfway through the tunnel, the nose velocity peak reduces by 30% compared to open air. The position of the nose inside the tunnel affects not only the slipstream velocity but also the velocity field at the tunnel portal and exit. These novel findings can be used as benchmark for designing new freight train and tunnel shapes.

**Keywords:** Computational Fluid Dynamics (CFD), Sliding-mesh, RANS, Flow separation, Compression wave, Train aerodynamics, k-omega SST

## 1. Introduction

Increasing the speed of freight trains has the potential to expand the capacity of the UK rail network, which is one of the reasons researchers have recently investigated the aerodynamics of freight trains.<sup>1, 2</sup> The importance of train speed arises from the fact that in general, aerodynamic forces increase in severity with the square of velocity.<sup>3</sup> In open air, the flow around the train, known as the slipstream, has been shown to produce higher slipstream magnitudes for freight trains when compared to passenger trains, primarily due to the bluff nature of the train shape. This finding combined with the fact that the train speed and shape<sup>4-6</sup> are believed to affect the pressure transients inside the tunnel, highlight the need to study the separated flow around a freight train in a tunnel.

When a train head enters the tunnel, it generates a compression wave, which reflects at the end of the tunnel as an expansion wave due to impedance mismatch (open-end piston effect). Then repeated pattern of pressure waves are formed, reflecting at each end of the tunnel.<sup>7-10</sup> The tail entry triggers the formation of an expansion wave leading to another pattern of reflective waves. Travelling at the speed of sound, these waves affect the pressure distribution around the train, contributing to additional drag inside the tunnel. The total additional drag is translated to a tunnel friction factor<sup>11</sup> which can be related to the drag coefficient in open air.<sup>12</sup> According to Vardy,<sup>13</sup> the drag of trains in tunnels include friction and pressure drag. Skin friction depends on blockage ratio, train length and surface roughness while pressure drag is generated by the pressure waves.<sup>13</sup> One of the main causes of drag inside the tunnel is pressure stagnation losses believed to occur at the nose of the train.<sup>14</sup> Consequently, these effects have driven many researchers to study the optimum nose shape for passenger trains aiming to reduce the strength of the initial compression wave which has the highest pressure amplitude.<sup>4</sup> However, due to the blunt nature of many freight train noses, combined with the need for higher train speeds, it is believed that the flow around freight trains is an increasingly important area of research. The flow at the head of a freight train can be related to a bluff body where it separates at the front part, forming a vortex, which is followed by a stagnant air region. Then, the flow curves back to the surface forming a reverse flow region.<sup>15</sup> The generation of turbulence occurs mainly in the reverse flow region.<sup>16</sup> This above phenomenon is called the separation bubble and can be either pressure or geometry induced. In general, flow separation causes energy losses (dissipated as heat) and deviation of streamlines.<sup>17</sup> The generation of pressure drag is another consequence of flow separation.<sup>17, 18</sup>

However, aerodynamic drag is believed to have a remarkable impact on performance only in long tunnels.<sup>13</sup> In short tunnels (<1km), the generation of drag is mostly associated with passenger comfort, which is not applicable to freight trains. Similarly, flow separation is believed to have a significant effect on the slipstream velocity magnitudes at the sides of freight trains.<sup>19</sup> High velocity magnitudes can create slipstream forces, which are capable of interacting with trackside objects. To quantify the size of separation bubble, several studies have investigated the length and height of the bubble.<sup>20-24</sup> The length of the separation bubble is the distance between the point of separation and point of reattachment and its height is the distance between the surface and the point where the velocity is equal to freestream velocity. The mean bubble length and height decrease with increasing  $Re$  (attributed to outer flow layers activity)<sup>25</sup> and surface roughness.<sup>26</sup>

The above phenomena can be predicted using a variety of techniques. Current methods in train aerodynamics include analytical models, physical experiments (at both full and model scale) and numerical simulations.<sup>3</sup> The use of analytical models can prove difficult when choosing coefficients, which depend on the train/tunnel system as a whole<sup>27</sup> and detailed information about the flow separation cannot be obtained. Results from full-scale experiments are accurate (if performed correctly) but complex to conduct. Model scale physical experiments reduce complexity and offer cost efficiency compared to full-scale testing, usually using moving models for simulating the relative motion between the tunnel/ground to the motion of the train.<sup>2, 28</sup> The main advantage of moving models over stationary models in wind tunnels is accuracy.<sup>3</sup> On the other side, the use of Computational Fluid Dynamics (CFD) has the advantage of full resolution results for obtaining detailed information (i.e. for the separated flow over the train). Although validation with experiments is required in most cases, CFD plays a key role in train aerodynamics and it is widely used to analyse the effect of crosswind on trains<sup>29</sup>, slipstream around the train<sup>1</sup> and tunnel effects.<sup>30</sup> For the latter case, using moving zones to simulate the relative motion can give validated results. For example, the study of Huang, Hong and Kim (2012) obtained experimentally validated results using RANS for investigating the unsteady flow inside the tunnel.<sup>31</sup> When comparing different RANS models,  $k-\omega$  has been found to be best choice for predicting the reattachment length and mean velocity profile, providing very good agreement with DNS.<sup>32</sup> Other approaches include the use of LES (in the expense of higher computational cost), for which the results of Khayrullina et. al. and Hemida and Krajnovic indicated good agreement with experiments.<sup>30, 33</sup>

This study presents an investigation of a container freight train entering a tunnel through numerical simulations, using the sliding mesh technique in combination with unsteady RANS. The simulations will be validated against results from a series of model scale experiments.<sup>19, 34</sup> The aim of this study is to investigate how the transition into the confined space of the tunnel affects the separation levels around the train and the slipstream around it. The link between these two highlights the necessity of exploring their dependence. The lack of detailed data from previous studies for freight trains in tunnels makes this study essential. The results of this study can be used as benchmark for designing new freight trains and tunnels. Designing more aerodynamically efficient freight trains (i.e. reduced drag) can contribute to reducing CO<sub>2</sub> emissions, as less efficient modes of transport (such as road truck freight) can be replaced. Section 2 describes the CFD methodology and techniques used, leading to the validation of results with scaled experiments in Section 3. The analysis of results is presented in Section 4, showing the separation levels and velocity field around the train, in relation to the position of the train and pressure waves inside the tunnel.

## 2. Methodology

### 2.1 Geometry

A simplified 1/25<sup>th</sup> scale model Class 66 locomotive connected to 8 flatbed wagons loaded with containers has been used, combined with a circular tunnel of constant radius. The use of container freight reflects the fact that it is amongst the largest freight sections in the UK.<sup>2</sup> The locomotive has a maximum length, height and width of 0.85m, 0.156m and 0.106m respectively (scaled dimensions). The bottom surface of the locomotive and container wagons have been significantly simplified, represented by a fully filled box. It has been found that for the flow around a Class 66 locomotive, simplifications at the bogie of the train do not prevent from obtaining slipstream magnitudes which are comparable to the real full-scale train.<sup>19</sup>

The focus of this study is on the upper part of the train, of which the shape is identical to the full-scale train. It has been ensured that the nose shape has been retained for a valid computation of the pressure transients. The simulation starts with the train nose located 8 meters away from the tunnel portal, replicating the experimental conditions. The orientation of the coordinate system can be seen in Figure 1. The origin of the vertical (y) and lateral (z) axis is at the ground and centre of the track respectively.

P1, P2 and P3 represent the measurement points used for the validation of pressure histories. The exact location of these points is given in section 3.2.

The same figure shows the location of measurement lines L1-L7 which are used for analysing the separation around the locomotive. The location of these lines in relation to the locomotive height is given in Table 2.

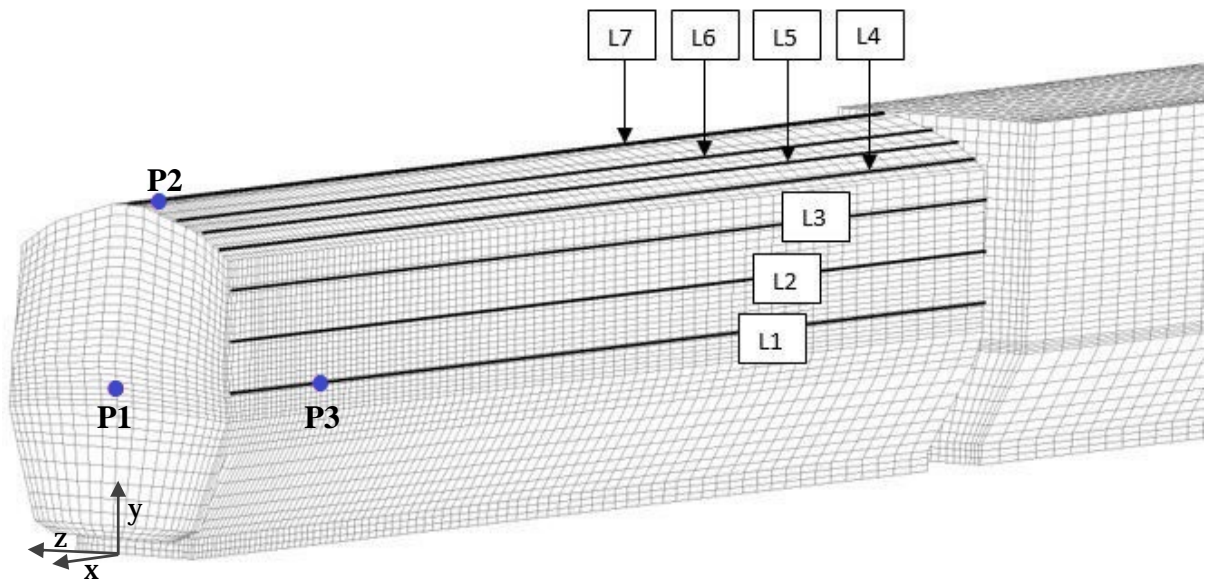


Figure 1: Computational model showing the surface mesh, data lines and measurement points

## 2.2 Similarity criteria

The scale of the model is  $1/25^{\text{th}}$  for ensuring minimum Reynolds number (ratio of inertia to viscous forces) effects, in line with the European Standards<sup>11</sup> for aerodynamic tests. Additional evidence on the above statement comes from the study of Johnson and Dalley<sup>35</sup> who confirmed that the use of this scale gives accurate pressure amplitudes inside the tunnel, when compared to full scale measurements. Regarding the flow around the train, Soper<sup>19</sup> suggests that the growth of the boundary layer and magnitudes of pressure and velocity in open air are comparable to full scale. This is however limited by the fact that the dissipation occurs at different scales when scaling the model. The above statement imposes that the scaled model used in this study can be used to highlight important characteristics of the separated flow around the train, but it is accepted the full-scale flow may differ at an acceptable level.

The pressure amplitudes inside the tunnel remain the same when converting to full-scale, but the time base needs to be multiplied by the scale ( $25\times$ ). According to CEN (2010) the full-scale speed must be retained for speeds up to 0.3 Mach.<sup>11</sup>

## 2.3 Sliding mesh method

The sliding mesh technique allows for the relative motion between the train, ground and tunnel. The moving domain slides along the stationary domain in the longitudinal direction with a speed of 33.5 m/s, where the location of the former is updated at each timestep. The two domains exchange information at a Generalized Grid Interface (GGI) (non-conformal fluid to fluid interface) that connects them (see Figure 2). The use of GGI allows the transfer of data between two faces of which their sizing does not match. At the interface, the fluxes are treated fully implicitly and there is conservation of mass, momentum, energy, scalars and other properties. More details about the GGI interface used on the sliding mesh technique can be found in the CFX Modelling Guide and the study of Liu, Hemida and Liu (2014).<sup>36, 37</sup>

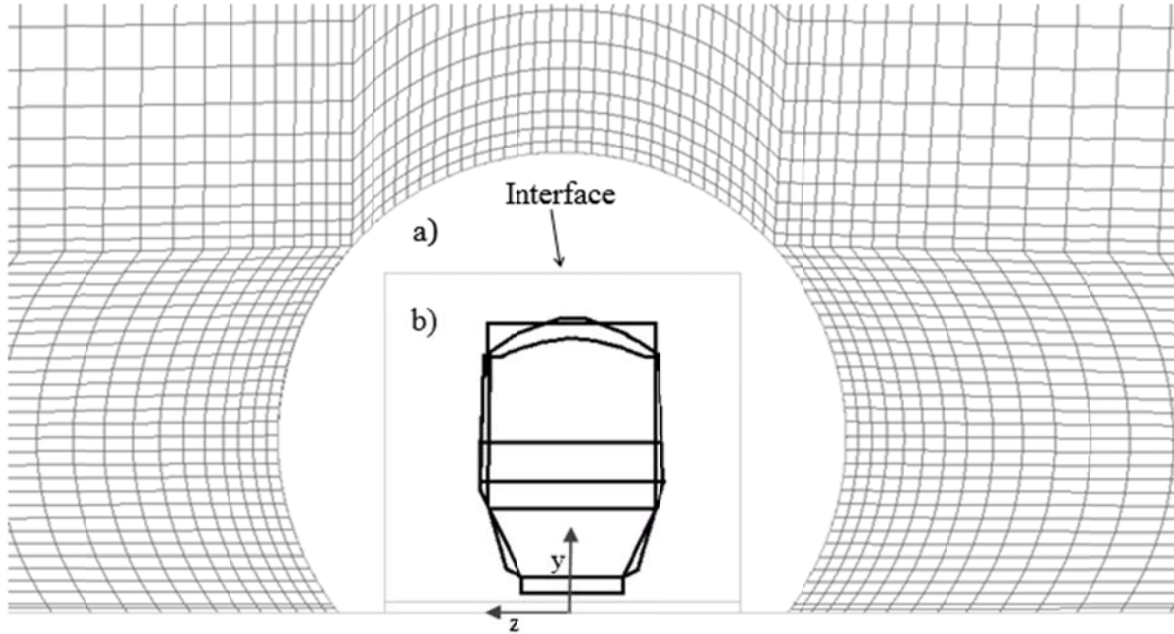


**Figure 2: Fine mesh at the entrance wall. The interface is where the moving and stationary domains connect a) Stationary domain; b) Moving domain**

## 2.4 Domain discretization

The structured hexahedral mesh shown in Figures 1-3 has been created in ICEM CFD using H-topology for alignment between the grid and flow, improved convergence and reduced CPU time. All edges use a node expansion ratio less than 1.2, which is constant along its length. The sizes of cells near the interfaces allow a smooth transition between the two domains. The moving mesh is finer near the train nose to capture the fine scales of the thin separated bubble region.

## 2.5 Numerical setup

The two-equation model  $k-\omega$  SST has been implemented because of its capability to predict separated flow under adverse pressure gradients. It provides accuracy and robustness on near wall treatment and switches to  $k-\epsilon$  in the freestream regions, showing lower levels of sensitivity to inlet boundary conditions. Considering the separation around the train head, SST is an effective choice as the automatic near wall treatment of the commercial code used (Ansys CFX) ensures the smooth transition from  $k-\omega$  (near wall) to  $k-\epsilon$  (free-stream). It models the transport of turbulent shear stresses through a modified turbulent viscosity formulation. The heat transfer modelling is using total energy where the transport of enthalpy and kinetic energy effects are modelled. The compressible flow simulation (density based on ideal gas law) is unsteady over a total time of 1.3s (the time required for the train to pass through the tunnel) with a constant time step of 0.0001s. The high-resolution advection scheme used is a 2<sup>nd</sup> order accurate implicit scheme while Second Order Backward Euler has been used for this transient simulation.

The surface mesh on Figure 3 shows the dimensions and boundary conditions applied to the pre-entrance domain. Identical dimensions and conditions have been applied at the post-exit domain. At the outlets, the flow is normal to the boundary with boundary conditions  $P=0$  Pa,  $T=288$  K and  $I=5\%$ . The outlet boundaries are located far from recirculation areas to simulate



the experimental conditions. All walls are adiabatic for preventing heat transfer across the boundary. The domain has been initialized with  $P=0$  atm,  $T=15^{\circ}\text{C}$ ,  $U_x=U_y=U_z=0$  m/s,  $I=5\%$ .

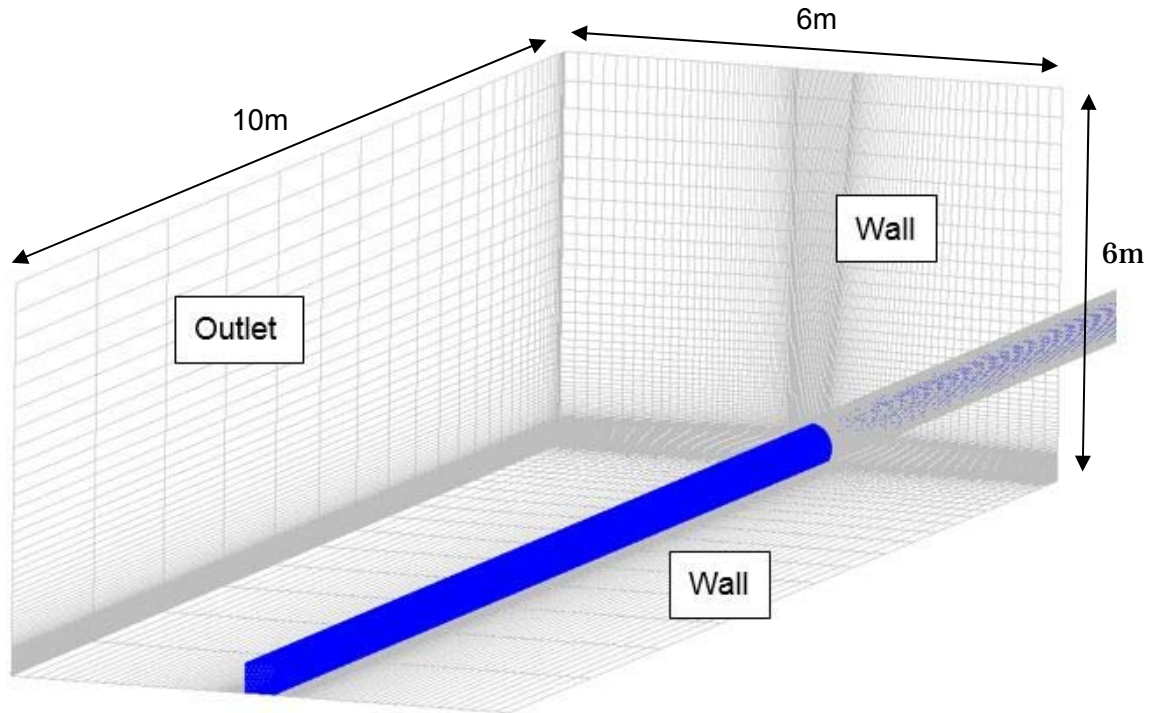


Figure 3: Boundary conditions at the pre-entrance domain. The blue region represents the moving domain. Identical boundary conditions have been applied at the post-exit domain. The remaining outlet faces which surround the pre-entrance domain are hidden.

Table 1: Geometric and flow parameters – Full scale unless stated otherwise

Locomotive	Class 66
Container wagons	FEA Type-B
Number of wagons	8
Total train length	182m
Model scale	$\frac{1}{25}$
Train cross-sectional area	$9.08\text{m}^2$
Tunnel length	574.5m
Tunnel cross-sectional area	$45\text{m}^2$
Train speed	33.5m/s
Re	384,000
Characteristic length (scaled)	0.156m (height of the scaled train)



Blockage ratio	0.202
----------------	-------

## 2.6 Experimental data for validation

The validation of results uses data from two studies that were conducted at the TRAIN Rig, using the model shown in Figure 4. This is a scaled ( $1/25^{\text{th}}$ ) Class 66 locomotive connected to eight FEA Type-B container wagons (except for the train surface pressure histories in section 3.2 which used four wagons). The model is fired by a mechanical propulsion system, following which it travels through a steady speed section where the measurements take place. The model is brought to rest using a piston deformable tube braking system. The region underneath the experimental model is less simplified compared to the computational model. More details about the facility and model can be found in the study of Soper et al.<sup>2</sup> All measurement positions are the same between the two experimental studies and the current computational simulations (see section 3 for more details).

For the validation of pressure histories, the experimental results from another study conducted by the authors of this paper have been used (see section 3.2).<sup>34</sup> Under the same flow parameters, pressures were recorded using  $\pm 2500\text{Pa}$  range pressure transducers, averaged over 3 and 15 runs at the tunnel walls and train surface respectively (to ensure repeatability). For these pressure measurements, some level of uncertainty can be expected from the position of train surface sensors (estimated to be  $\pm 1\text{mm}$ ) and a maximum train speed deviation of 1%. As mentioned above, the train surface pressures were only available from a shorter train, thus the comparison starts in open air and finishes before the four-wagon tail enters the tunnel.

In section 3.3, the velocity field is validated with results taken from the study of Soper.<sup>19</sup> In this study, velocities were recorded using Cobra Probes with a sampling rate of 2500Hz. Potential uncertainty comes from instrument positioning accuracy of  $\pm 1\text{mm}$  and  $\pm 2^\circ$ . The measurements were conducted in line with the CEN requirements and the velocity results were averaged over a minimum 25 runs.

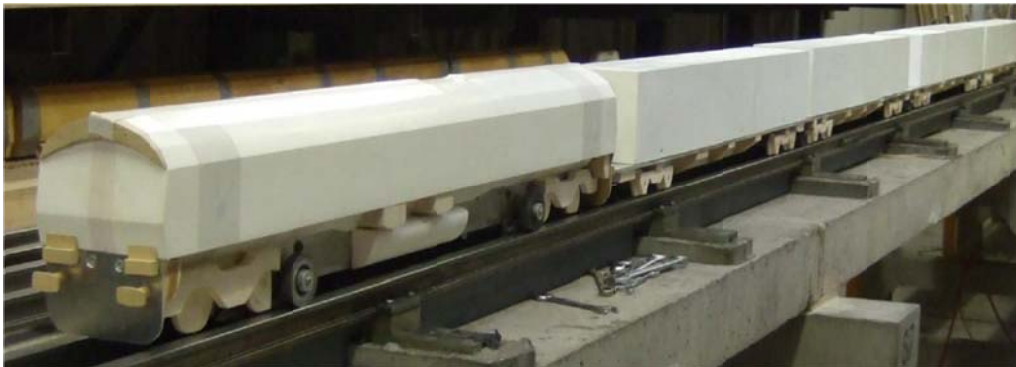


Figure 4: Experimental model at TRAIN Rig.<sup>19</sup>

### 3. Model Validation

#### 3.1 Timestep and mesh independence

For this timestep and mesh independence study, the pressure histories at the tunnel walls have been used. Figure 5 shows pressure monitored at two meters from the entrance (see vertical axis) against time, which has been kept in its scaled form (see horizontal axis). Figure 5a confirms that there is no effect on the initial compression wave when increasing the time step. Therefore,  $t=0.0001s$  has been used to keep the computational time to a minimum. Similarly, grid independence was obtained using three different densities;  $2.8 \times 10^6$ ,  $3.2 \times 10^6$  and  $4.2 \times 10^6$  elements named as coarse, medium and fine mesh respectively (see Figure 5b). These grids were generated with the same topology but different sizing to ensure consistency. The differences in the sizing of the three meshes are around the train and inside the tunnel. A mesh independent modelling of the pressure waves is important before validating pressure histories with experimental data. Figure 5b confirms that the solution does not change when increasing the mesh density (from medium to fine), as shown by the pressure histories at the tunnel walls. Therefore, the results presented from section 3.2 onwards have been obtained using the medium mesh.

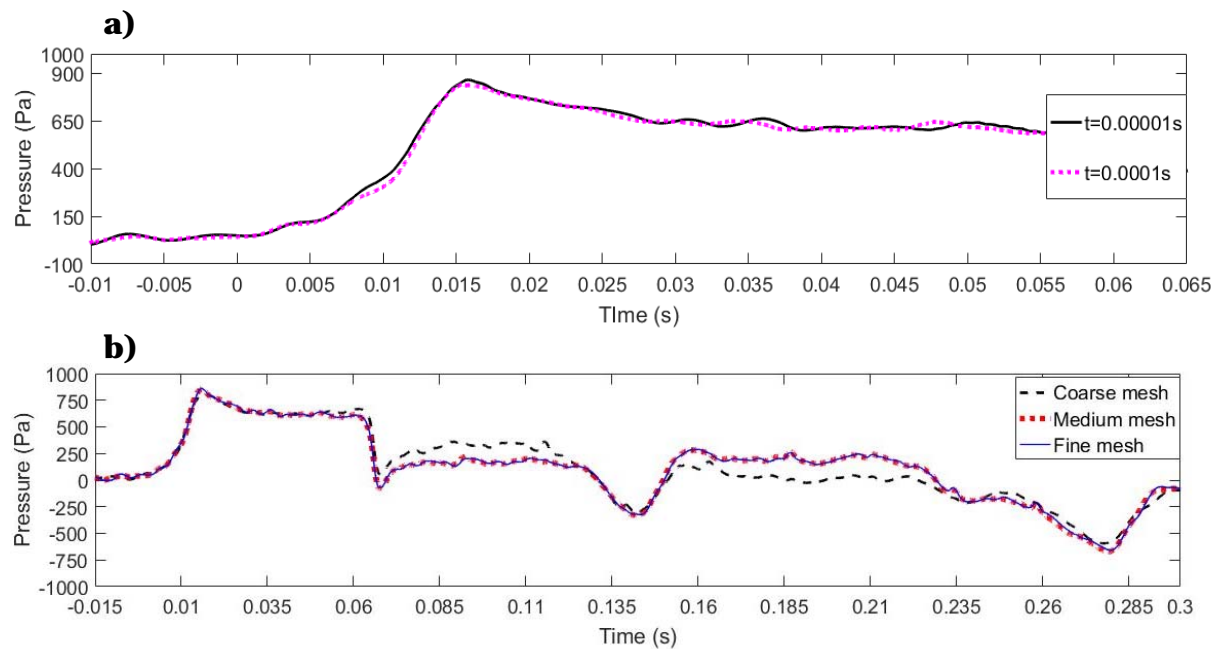


Figure 5: Pressure histories at the tunnel walls, two meters from the entrance a) Timestep Independence; b) Mesh Independence

## 3.2 Pressure histories validation

This section uses results from the physical tests described in section 2.6 to validate the numerical pressure histories. Figure 6 consists of three plots which represent the different monitored locations. For all three subplots, the time-base in the horizontal axis has been retained in its scaled form.

### **Tunnel walls**

This part of model validation aims to show the accurate modelling of the pressure waves. This allows for an investigation of the pressure transients effects on the separation levels or velocity field inside the tunnel. Figure 6a shows the pressure histories monitored at a fixed location, two meters from the entrance. Pressure starts increasing when the train approaches the tunnel and enters the tunnel (at  $t=0$ s). The first significant increase is observed by the compression wave generated by the nose entry, which travels towards the tunnel exit with the speed of sound. This is the highest amplitude among all pressure changes. The gradient of this initial compression wave is captured with 100% accuracy. The initial pressure wave amplitude is under predicted by 10% justified by dissimilarities in the train speed and potential differences in the blockage ratio. Regarding the former, due to the nature of the experiments, the results are ensemble averaged over 15 samples/runs with a maximum speed deflection of 1%. The latter can be explained by differences between the simplified underbodies of the two models which can affect the train cross-sectional area. The first significant pressure drop is caused by the train nose passing by the measurement point at approximately  $t=0.06$ s. The air is suctioned as the train approaches the measurement point and displaces the air. The negative peak is captured successfully indicating accurate modelling of the air suction.

For  $t \geq 0.5$ s, the pressure changes occur earlier in the numerical simulation. This inconsistency is explained by the speed difference between the two approaches, which influences the timing of the pressure waves. A speed reduction during this period could delay the tail entrance and the generation of the second pattern of pressure waves.

The pressure amplitudes reduce with time as the sound waves energy is consumed by frictional effects. The numerical model confirms that the waves continue to reflect at the two portals until the energy is dissipated, even after the train tail has exited the tunnel. This is caused by friction effects and emission of micro-pressure waves.

In summary, the numerical method adopted shows satisfactory agreement with experimental results for the pressure waves inside the tunnel. Therefore, this methodology can be successfully implemented to model the pressure transients inside the tunnel. In addition, compliance against current requirements for trains in tunnels can be checked, although this is not the focus of the current study. The TSI requirements are specified in terms of the maximum gradient and amplitude of the initial compression wave.<sup>38</sup>

### **Nose, roof and side**

Figure 6b and Figure 6c show the pressure histories at the locomotive surface, in open air and inside the tunnel. Pressure was monitored at P1, P2 and P3, which are located at the nose, roof and side of the locomotive surface respectively (see Figure 1 for an illustration of their location). P1 is located at the nose (middle height and centre of the track), while P2 is located

at the highest point of the locomotive roof (on L7) and 3.4% of its length. The location of P3 is at the middle height of the locomotive (on L1) and at 14% of its length.

At P1, the positive pressure in open air is attributed to air stagnation (see  $t=-0.05$  to  $t=0$ s in Figure 6b). At  $t=0$ s, the confined space of the tunnel and compression wave generated ahead of the nose cause the sudden pressure change. Pressure increases to approximately 1500Pa, which is captured with 97% accuracy by the numerical model. In general, excellent agreement between experiments and CFD is found for this measurement point.

For P2 and P3, the open air pressure is negative at the roof and side of the locomotive, attributed to flow separation (see Figure 6b and Figure 6c). These two measurement points are located within the separated flow zone, between the separation and reattachment point. When the nose enters the confined space of the tunnel, P2 and P3 increase towards zero because of the instant interaction with the tunnel portal. This increase is recorded between  $t=0$ s to  $t=0.02$ s on the horizontal axis of the same figures. The most remarkable differences between experiments and CFD are observed for this time period. A potential explanation for this difference is geometrical differences at the tunnel portal. After this relatively instant phenomenon, pressure stabilises between  $t=0.02$ s and  $t=0.12$ s, where the separation length establishes. The pressures for this period are higher than the open air pressures which is explained by the change in the location of the reattachment point. More specific, across the separation length, pressure is almost minimum at the separation point and then increases as it approaches the reattachment point.<sup>39</sup> Inside the tunnel, the separation bubble is shrunk and therefore P2 and P3 are closer to the reattachment point. This is translated to higher pressures at these monitored locations. As shown in Figure 6b and 6c, the numerical model captures with satisfactory agreement the values of both P2 and P3 during this time period ( $0.02\text{s} < t < 0.12\text{s}$ ).

The disagreement between experiments and CFD is higher for P3 compared to P2, explained by the fact that P3 is closer to the underbody of the locomotive where dissimilarities in the underbody of the two models exist. The speed difference can potentially explain part of this disagreement.

For all three measurement points, the results confirm previous findings that pressure is constant in open air but varies inside the tunnel.<sup>13</sup> This has also been confirmed by a recent study which showed that the pressure variations on the train surface are caused by the pressure waves.<sup>34</sup> Although an in-depth analysis of the pressure field is out the scope of this paper, the validation of pressures within the separation zone presented here, shows accurate modelling of the boundary layer phenomena. The agreement between the numerical model and experiments in Figure 6 validates the adopted method for this numerical study.

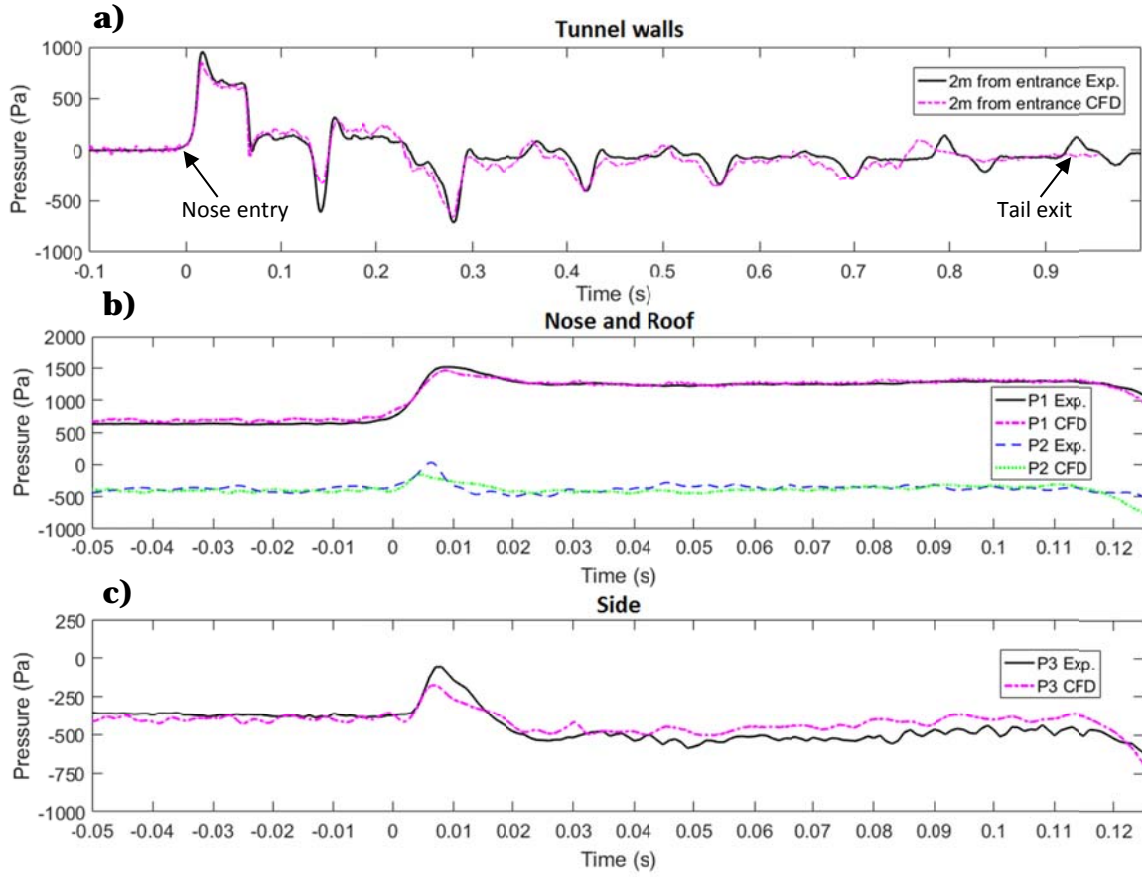


**Figure 6: Model validation of pressure histories using experimental data from Iliadis et al. (2018).<sup>34</sup> The nose enters the tunnel at  $t=0s$ ; a) Tunnel walls - 2 meters from the entrance; b) Nose and roof of the locomotive; c) Side of the locomotive**

### 3.3 Velocities around the train nose

Figure 7 shows the validation of the numerical model with scaled experiments, taken from the slipstream study of Soper.<sup>19</sup> The instantaneous velocity was recorded at L9, which is 0.09m and 0.07m (2.25m and 1.75m in full-scale) from the ground and centre of the track respectively. Figure 14 illustrates the position of L9 in relation to the train and tunnel. In the numerical results, due to the size of the pre-entrance domain, the train nose is located three meters away from the tunnel portal. Conversely, in the experimental measurements there is no tunnel ahead of the train. This is the only difference between the measurement positions in both methods. The longitudinal axis represents the distance from the train nose, which is positive towards the tail of the train, while the vertical axis shows the normalised velocity  $U_x/V$ .  $U_x$  is the longitudinal component of velocity and  $V$  is the train speed. The use of  $U_x$  is common practice for slipstream studies.<sup>40, 41</sup>

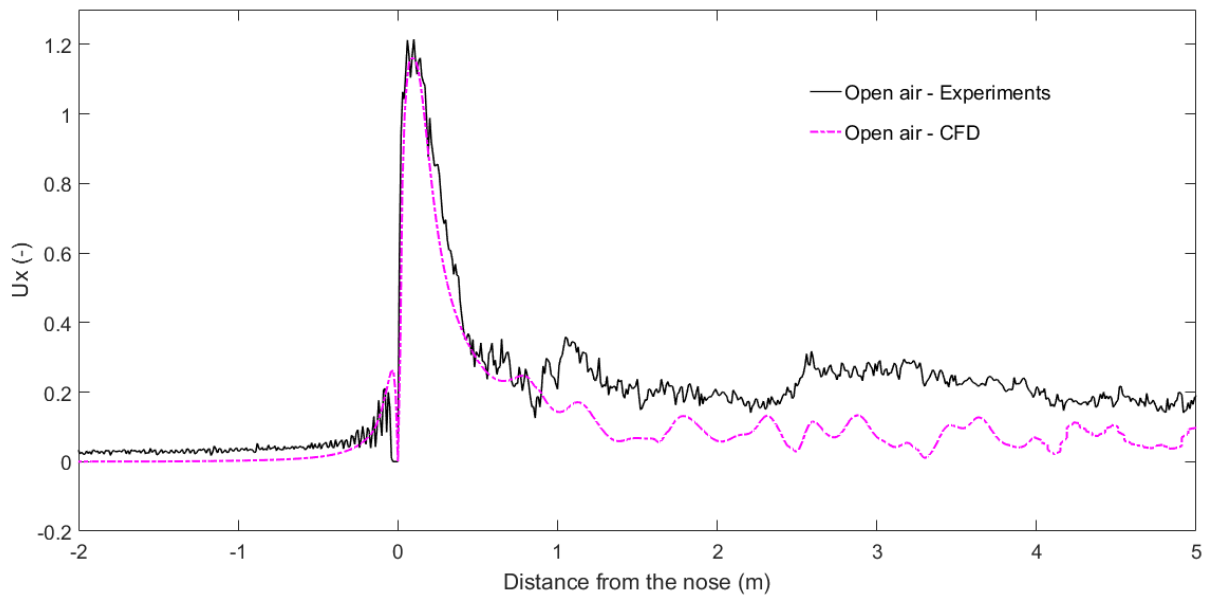


**Figure 7: Comparison with experimental results at L9.<sup>19</sup> Normalised longitudinal velocity across different distances from the train nose. The negative horizontal axis is aligned with the direction of travel.**

For reference, the flow around the train is divided into the upstream, nose and boundary layer regions, taken from a previous open air analysis of Baker et al. (2001) (the near wake and far wake regions are not analysed in this section).<sup>6</sup> In the upstream region (the negative side of the horizontal axis in Figure 7), the flow velocity is slightly higher than zero due to the displaced air ahead of the train and any differences between the two methods can be explained by the presence of tunnel entrance wall in the CFD model. In the experimental measurements, air is free to move without facing any opposition from the presence of a tunnel portal. Potentially, this explains the fact that the first small peak ahead of the nose is under predicted by the numerical scheme. In the nose region, the peak magnitude is predicted accurately by the CFD model with a difference of 4.5% while its gradient and length are captured with 100% accuracy. When moving further backwards, the level of agreement reduces near the boundary layer region. This can be potentially linked to differences between the two models in the underbody of the train, due to geometry simplification. Similar differences in this region were found in other CFD studies when comparing to experimental data.<sup>1</sup>

The prediction of the velocity peak at the nose is satisfactory to analyse the flow separation in this region, confirming the use of the CFD model suitability for this study.

## 4. Results and discussion

### 4.1 Separation over the roof and at the sides of the train

The analysis focuses on the separated flow at the sides and roof of the locomotive. To that end, the separation and reattachment points can be computed using the longitudinal component of wall shear stress  $\tau_w$ <sup>42</sup>, which is in this case is parallel to the inlet flow and train roof.  $\tau_w$  is the force per unit area applied to the fluid by the wall, defined as:

$$\tau_w = \mu \left( \frac{\partial u}{\partial y} \right)_{y=0} \quad \text{eq. 1}$$

At the point of separation and reattachment, it is commonly known that  $\left( \frac{\partial u}{\partial y} \right) = 0$ , derived from Navier-Stokes equations<sup>42</sup>. Calculating the nominal magnitude of  $\tau_w$  would give positive values only, therefore it is important to also consider the longitudinal component, plotted along the length of the locomotive (L). The sign of  $\tau_w$  depends on the coordinate axis, which in this case is opposite to the flow, producing positive values within the separated flow area. As noted before, the separation bubble length is defined as the distance between the point of separation and point of reattachment. Table 2 below shows the reattachment point recorded at various heights h of the locomotive and expressed in terms of its position along the locomotive length L (see Figure 1 for the location of each line). The unsteady RANS simulations showed that the reattachment points shown in Table 2 are time-independent as the separation length remains unchanged over time (both in open air and inside the tunnel). The analysis presented in this paper focuses only on one side of the locomotive, as negligible differences were found between the left and right sides of the tunnel.

**Table 2: Reattachment point – Open air and Tunnel**

	Line	Line position (% of h)	Reattachment point (% of L) Open air	Reattachment point (% of L) Tunnel	Change (%)
Roof	L7	100	25.1	17.0	32.0
	L6	96.62476801	23.0	17.0	26.0
	L5	93.9269429	20.5	15.2	26.0
Sides	L4	89.83657749	19.0	14.0	26.0
	L3	79.3253104	19	14	26
	L2	65.79018854	23.8	16.5	31
	L1	52.17358912	26.1	19	27



## Separation over the roof

Inside the tunnel, the flow deflection angle changes due to the presence of the tunnel walls which redirect the flow towards the train surface. Figure 8 shows the values of  $\tau_w$  along the non-dimensional locomotive length. The flow separates at the corners of the train head (origin of the horizontal axis), where wall shear stress is zero. After separation,  $\tau_w$  becomes positive because the flow has the same direction as the train, in alignment with the positive longitudinal axis of the coordinate system. Air flows towards the front of the train, indicating backflow at the core vortex. Behind this point, the reattachment of the separation bubble to the train surface occurs when the wall shear stress is zero again. When the train enters the tunnel, the separation point remains unchanged while the reattachment point moves towards the front (compared to open air). Consequently, the separation bubble length is reduced by up to 32% inside the tunnel. In the lateral direction, the most intense reduction in separation bubble length is found at the centre of the track, attributed to the extended corners of the train at this region. It can be observed that the higher the distance from the centre of the track, the shorter the separation length. This can be confirmed from Figure 11 which shows the levels of wall shear stress at the locomotive surface.

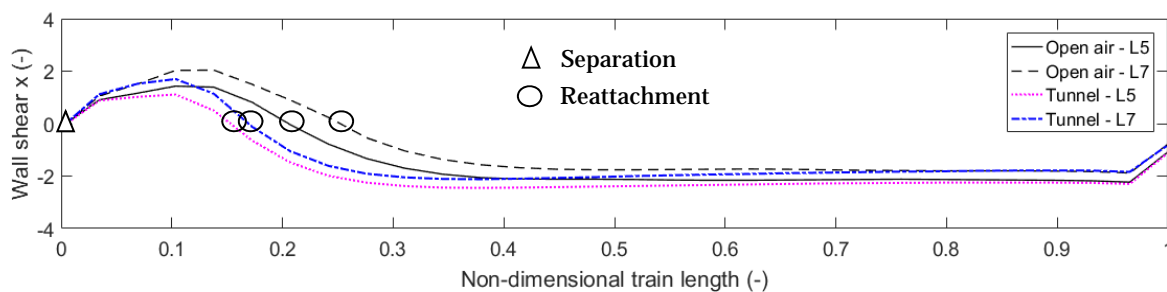


**Figure 8: Separation at the roof of the locomotive; Nose at 0 and tail at 1.**

After reattachment, within the recovery region, the values of  $\tau_w$  continue to drop. This is the region where a turbulent boundary layer starts building up gradually both in the longitudinal and vertical direction. Previous studies have highlighted that due to the nature of turbulence, mixing occurs at this area and turbulence intensity is high, but decreases with distance from the reattachment point.<sup>43</sup> As the distance from the separated flow increases, the boundary layer is not influenced by the upstream mixing flow and stabilises.

Post-recovery,  $\tau_w$  stabilises to constant values which indicates a turbulent boundary layer is formed, between 52 and 97% of the locomotive length at the sides and between 39 and 97% over the roof. The size of the boundary layer in the vertical direction is believed to be constant within this region and significantly smaller than the height of the separation bubble<sup>17</sup>. Moving towards the rear, at 97% of the locomotive length, the flow separates again due to the sudden gap between the locomotive. Similarly to the train head, this is a geometry induced separation and its location is not affected by the tunnel walls and remains unchanged after the train entry.

Figure 9 shows the velocity profile across L8, which is a vertical line at the maximum height of the separation vortex), at the centre of the track ( $z=0$ ). In open air, this occurs at 70% of the separation vortex length, and inside the tunnel at 63%. The longitudinal component of velocity is normalised with train velocity  $V$  and plotted against the distance from the highest point of the roof ( $y$  minus  $h$ ). The velocity sign has been adopted in the direction of the coordinate system for illustration purposes. The negative curved profile shows an adverse pressure gradient within the separated flow. The height 'H' of the separation bubble is

defined as the distance from the inflection point to the wall, which is within the boundary layer.  $H$  is slightly lower inside the tunnel, compared to open air. Outside this region (between 0.028m and 0.075m on the vertical axis of Figure 9), the freestream velocity is higher in the tunnel due to the reduced cross-sectional area causing flow acceleration. The negative velocities within the vortex indicate backflow of significant strength which remains unchanged during train entry.

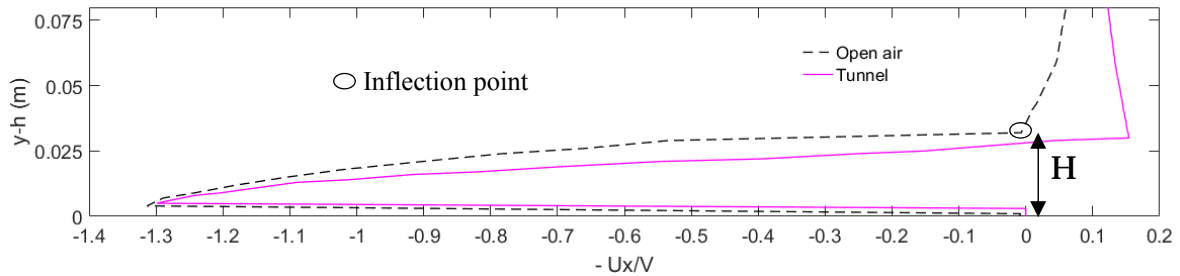


**Figure 9: Instantaneous normalised velocity profile along L8;  $z=0\text{m}$  (centre of the track). The location of L8 can be seen in Figure 11.**

### Separation at the sides

Figure 10 presents the variation of separation length at the sides of the train, by comparing measurement lines L1 and L3 in open air and inside the tunnel. As shown, the maximum separation length is found at 52% (L1) of the train height (both in open air and inside the tunnel). This reduces when moving towards the roof of the train as the locomotive width reduces gradually above the middle height. This indicates that the wider shape of the train head, the longer the separation bubble. This is identical to the separation over the roof, where the extended edge of the train head in the vertical direction produces the maximum separation. The edges affect the gap between the locomotive and tunnel walls, changing the deflection angle at separation. Therefore, it is believed that the above observations depend highly on the tunnel shape.

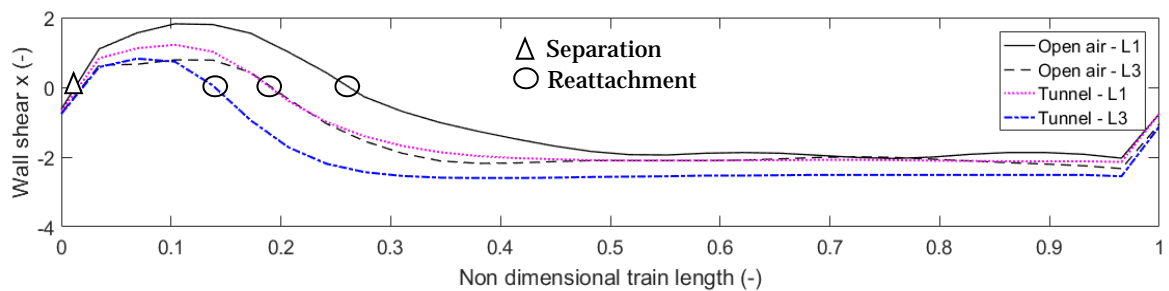


**Figure 10: Separation at the sides of the locomotive; Nose at 0 and tail at 1.**

The findings discussed above can be confirmed from Figure 11 which shows the contours of  $\tau_w$  along the locomotive surface. The maximum separation levels at the sides and roof of the train are identical; with slightly longer separation levels on the latter (see Table 2). Although the separation length at the bottom of the train is significant, this is believed to be because of the fully filled underbody of the train, used for the purposes of this study.

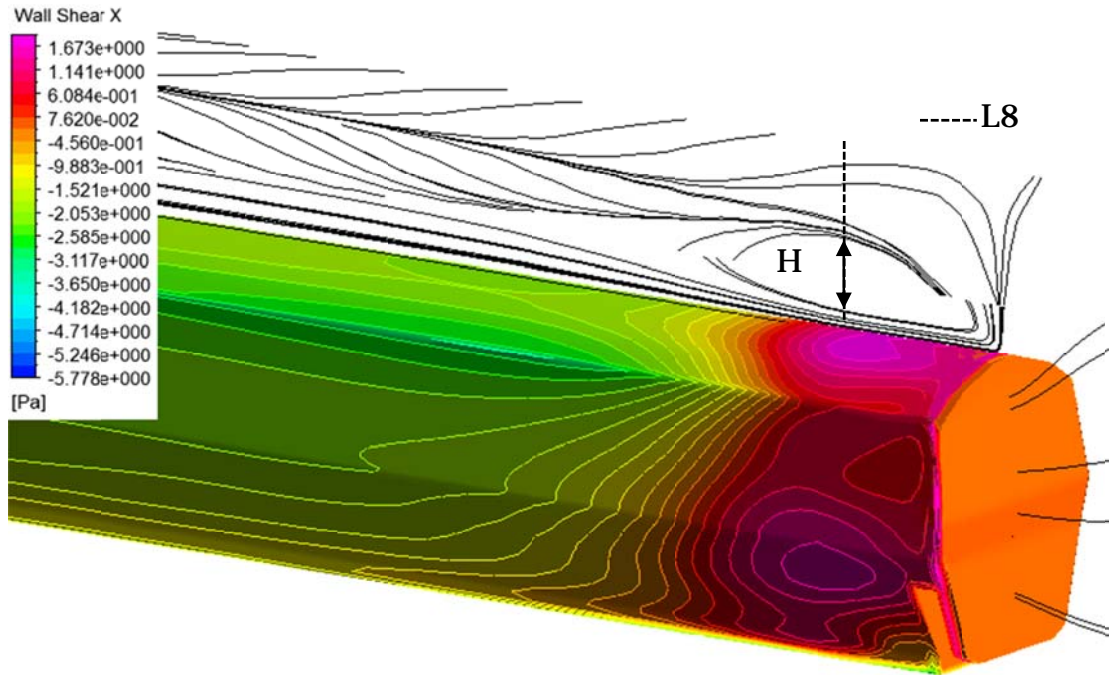


Figure 11: Wall shear stress contour and surface streamlines inside the tunnel, showing the height of the separation bubble and the vertical velocity profile; (see Figure 9)

### Time-dependence of separation

The unsteadiness of the flow around the train can be related to the nature of separating and reattaching flows which exhibit low-frequency unsteady behaviour<sup>44</sup> and to the effects of the transient pressure waves. In practical terms, unsteadiness in the flow is related to the generation of vibration and noise.<sup>45</sup>

Figure 12 indicates that the points of separation and reattachment (when  $\tau_w=0$ ) remain unchanged across different instants. However, the velocity field is different at the two instants, due to the turbulent nature of the flow (evident from the values of wall shear stress before and after reattachment). Mixing occurs, affecting the circulating flow. This is translated to changes within the core vortex and the dead air region behind it. Moving further backwards, the fully developed turbulent boundary layer downstream of the reattachment point experiences different velocity gradients. However, the separation point at the rear of the locomotive remains unchanged.

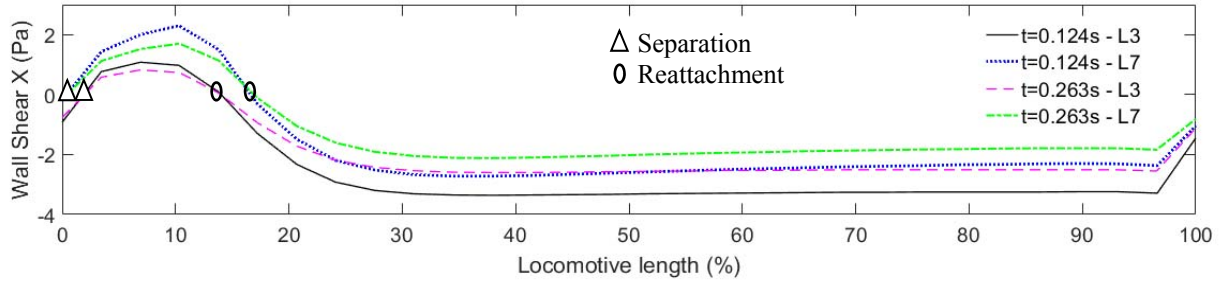


Figure 12: Wall shear stress at different instants inside the tunnel

## 4.2 Velocity field around the train

As shown in the previous sections the separation length between the roof and the sides of the train vary. Similar differences have been observed for the velocity field by Soper et al. (2015) who found that the longitudinal component of velocity  $U_x$  is higher at the sides than at the roof.<sup>46</sup> Based on the above, the analysis of the velocity field in the study focuses on the sides of the train only.

All results have been extracted from line L9, which is shown in Figure 14 and its location was given in section 3.3.

### Flow around the nose

The vertical axis in Figure 13 shows the longitudinal component of velocity at L9, normalised with the train speed. On the horizontal axis is the distance from the train nose, where the tail of the first car (locomotive) is approximately at 0.82m

In the upstream region (negative axis), velocity is slightly increased because of the displaced air ahead of the nose. When the train nose is in the middle of the tunnel length, the upstream velocity is significantly higher than in open air due to the restricted space inside the tunnel and the presence of pressure waves. The upstream velocity is 25% of the velocity peak at the nose.

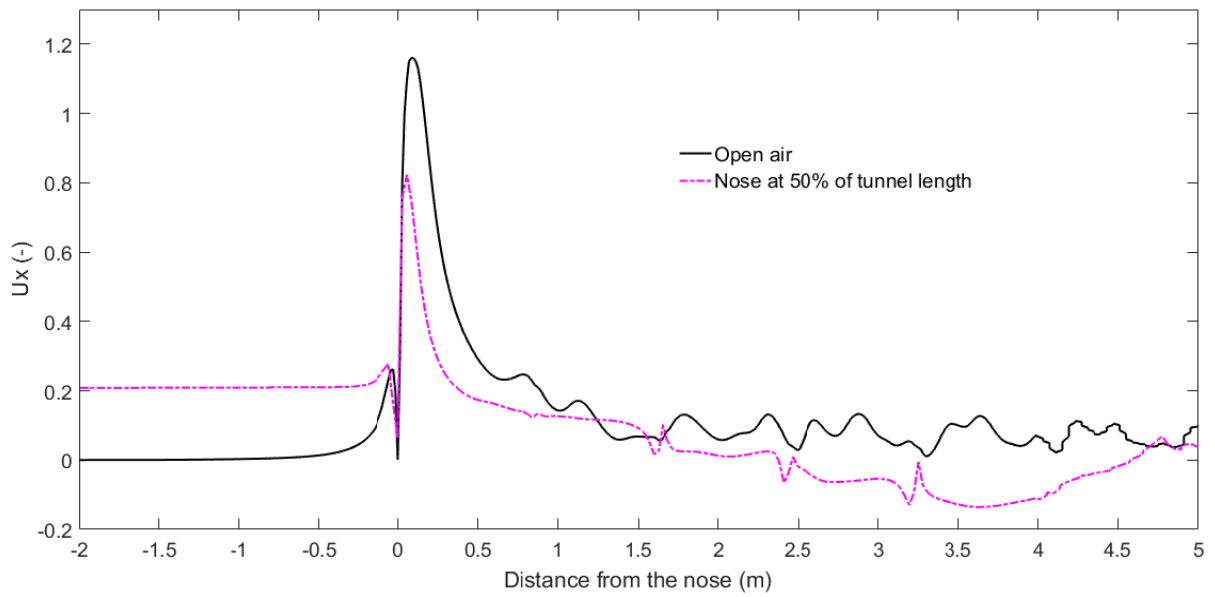


Figure 13: Normalised Longitudinal component of velocity recorded at line L9. The distance is positive towards the tail and negative towards the direction of travel (distances in scaled form)

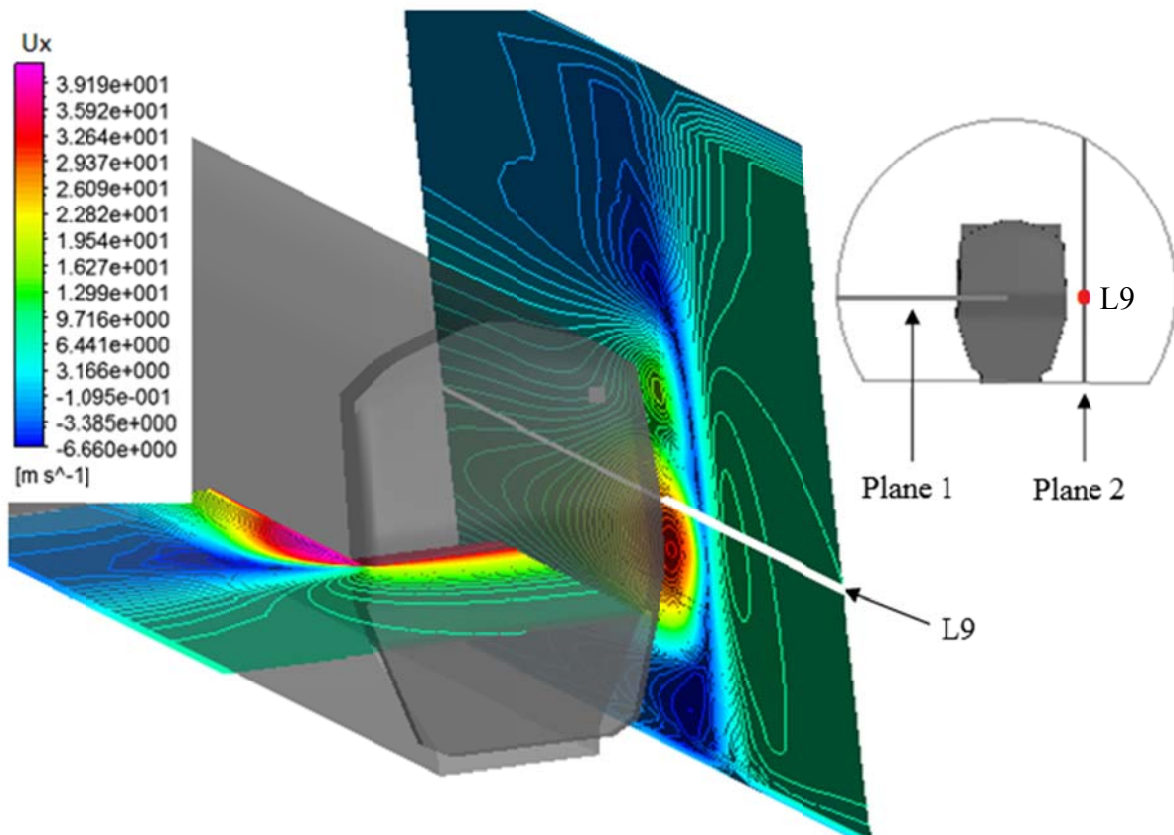


Figure 14: Contour of longitudinal component of velocity around the nose inside the tunnel. Planes 1 and 2 are located 0.09m and 0.07m (2.25m and 1.75m in full-scale)

from the ground and centre of the track respectively. Measurement line L9 is located on Plane 2.

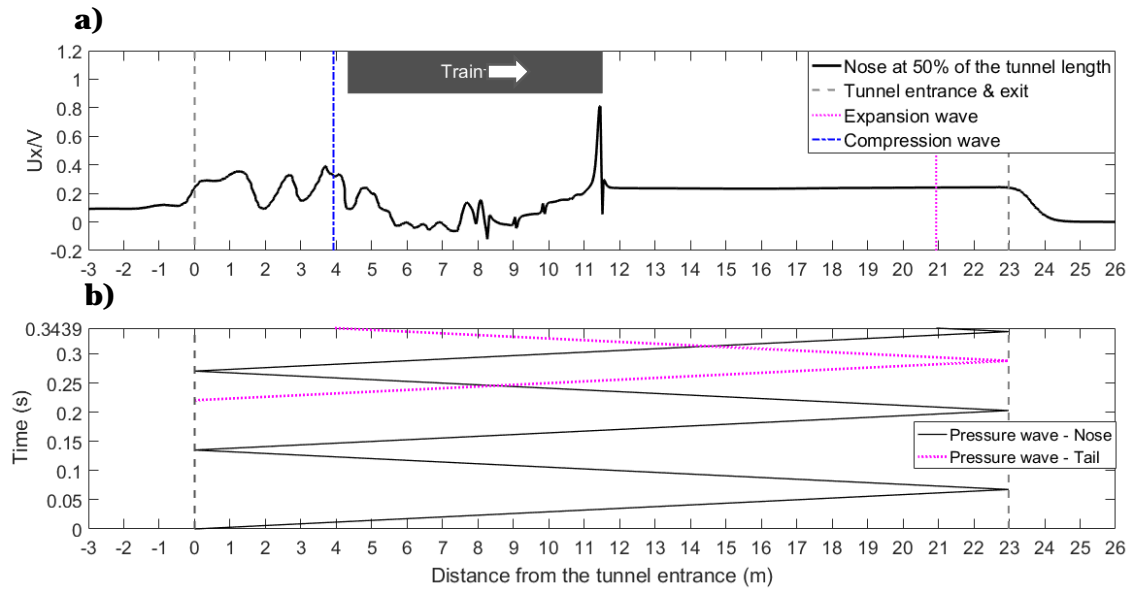
The open air peak velocity at the nose region is higher than the train speed by 20%. From Figure 13, it is evident that the magnitude reduces by 30% when the train is inside the tunnel. Similarly, the peak length is shorter, attributed to the shorter separation bubble inside the tunnel.

Figure 14 confirms previous research findings which suggest that the velocity magnitude is related to flow separation around the train and reduces when the distance from the centre of the track increases, both on passenger<sup>47</sup> and freight trains<sup>46</sup>. Plane 2 on Figure 14 illustrates that the maximum nose velocities are found near the middle-height of the train, where the locomotive corners are closer to the measurement point (L9).

Within the boundary layer region, velocity is relatively stabilised due to the homogeneous geometry of the wagons. Soper et al. (2015) found that when the train is partially loaded with container wagons, the leading faces of the containers cause additional velocity peaks making the flow more complex.<sup>2</sup> Although there are no significant fluctuations in the results of the current study in the boundary layer region, any small size effects can be explained by the gaps between the containers.

### Velocity dependence on the location of the train and pressure waves

Figure 15a shows the instantaneous normalised velocity extracted from L9 at  $t=0.3439s$ , along the length of the tunnel in relation to the position of the train and the pressure waves. This instant has been selected based on the fact that a compression wave has just passed from the train tail and therefore, its influence on the velocity field around it can be detected. In addition, the selected time ensures that the train is well inside the tunnel, allowing analysis of the velocity field around the whole train length. The development of the pressure waves until this instant are shown in Figure 15b. This figure shows that the first pattern of reflective pressure waves starts at  $t=0s$  as a compression wave reflecting at the tunnel exit at  $t=0.0676s$  as an expansion wave. Similarly, during the tail entry the second pattern starting at  $t=0.2204s$  is an expansion wave which reflects back as a compression wave. During the instantaneous snapshot at  $t=0.3439s$  shown in Figure 15a, there is a compression and expansion wave present in the tunnel, behind the tail and far away from the nose respectively.



**Figure 15: a) Normalised longitudinal component of velocity at L9 at  $t=0.3439s$ ; b) Location of the pressure waves with time. The nose enters the tunnel at  $t=0s$ .**

Apart from the nose peak, the slipstream velocity values between the nose and tail are lower than the rest of the graph and in some cases negative. These effects are believed to be linked to the position of the probe being within or very close to the separated flow along the train which causes energy losses. The lowest negative slipstream velocities are found at approximately 50% of the train length.

Figure 15a shows the train nose halfway through the tunnel length. At the rear part of the train, the first velocity increase occurs at the tail and after this point velocity levels are maintained with the presence of some fluctuations. On the other side, when the nose is at 88% of the tunnel length, velocity reduces significantly after the first velocity peak (see Figure 16). Therefore, the high slipstream velocities behind the tail when the nose is halfway through the tunnel length can be potentially related to the presence of the compression wave at this region, as shown in Figure 15.

The same figure suggests that the expansion wave does not have any effect on the velocity along the recorded line, as it remains unaffected in front and behind the wave.

### Time-dependence of velocities

Figure 16 shows the normalised velocity inside and outside of the tunnel at different snapshots. Outside of the tunnel, the velocities at the exit and entrance are important because of the occurrence of micro-pressure waves and exiting vortex jets respectively.



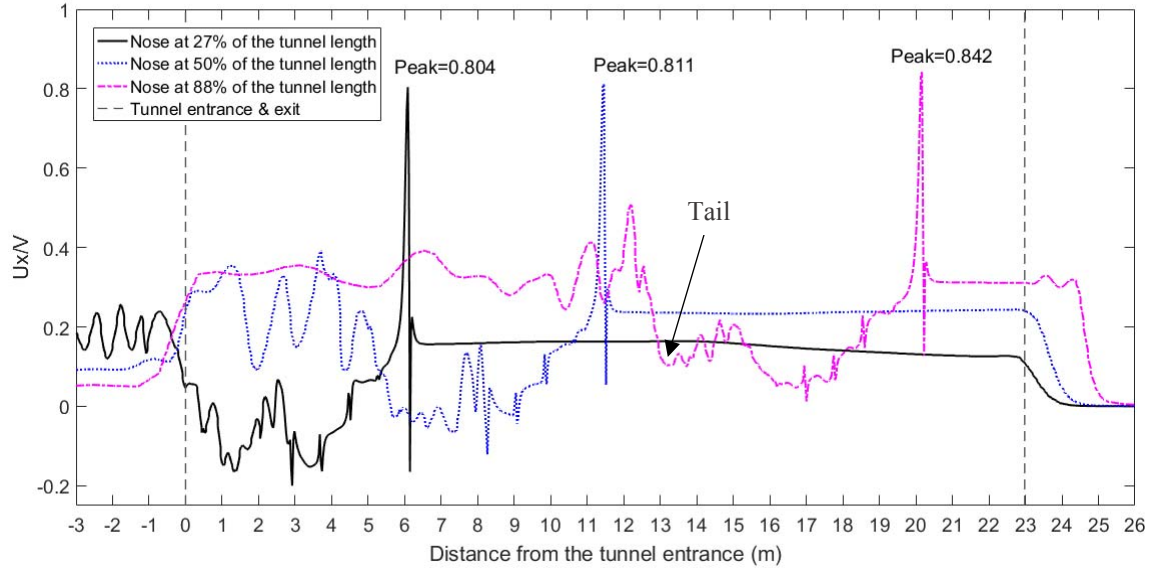


**Figure 16: Normalised longitudinal component of velocity at  $t=0.1839s$ ,  $0.3430s$  and  $0.6038s$**

Figure 16 shows that as the train moves away from the tunnel entrance, the following effects are observed:

- The velocity magnitude at the nose increases.
- The velocity ahead and behind the train increases.
- The velocity at the exit of the tunnel increases as well as the area of influence outside the tunnel. For example, when the nose is at 88% of the tunnel length, it affects the air as far as 2.5 meters away from the exit. The closer the nose to the exit, the higher the velocity of the displaced air ahead of the train.
- The air velocity near the tunnel entrance reduces.

The presence of the wake behind the train increases when the train moves away from the entrance, causing flow acceleration inside the tunnel. As a result, this increase in velocity in the tunnel affects velocities a-c above. On the other side, effect d can be linked to the fact that when the train moves away from the tunnel entrance, the influence of the wake on this region is less significant.

## 5. Conclusions

This novel study investigated the validity of using the sliding mesh technique to assess the aerodynamic flow development and analysed for the first time the flow around a Class 66 locomotive connected to eight container wagons passing through a tunnel with a blockage ratio of 0.202. Unsteady RANS simulations were performed and the results were validated with experimental measurements. The results presented here can be used by freight train designers to compare improved nose shapes, as detailed data about the separation length and velocity distribution around freight trains in tunnels were not available in the literature until now. A series of important conclusions are summarised below:

- The gradient of the initial compression wave is calculated accurately while its pressure amplitude is estimated with 10% difference from the experiments. The differences are attributed to differences in the train speed of the two

simulations. The CFD model in general exhibited good agreement with experimental results.

- The k-omega model predicts the pressure waves amplitude for the remaining of the pressure traces showing satisfactory modelling of the friction effects.
- The pressure histories at the locomotive nose, roof and side were validated with experimental data showing correct modelling of the boundary layer phenomena.
- The velocity peak at the train nose is captured with 95.5% accuracy while its gradient and length are captured with 100% accuracy. This confirms the validity of the adopted method.
- When the train enters the tunnel, the reattachment point of the separation bubble reduces by 31% and 32% at the sides and roof of the train respectively.
- The separation bubble is largest at the mid-longitudinal and mid-lateral planes of the train, explained by the extended edges of the locomotive at these regions. Inside the tunnel, at the sides of the train, the longest separation bubble is found at 52% of the train height where it reattaches at 19% of the locomotive length.
- The flow separates again at the rear part of the locomotive (97% of its length) due to the space between wagons. This separation point remains unchanged when the train is inside the tunnel.
- The velocity profile along the vertical direction of the separation bubble showed an adverse pressure gradient, backflow of significant strength (130% of the train speed) and identical height of the bubble in open air and inside the tunnel.
- The separation at the roof and sides of the train increases with distance from the centre of the track and from the centre of the locomotive height respectively.
- Close to the train side, the nose slipstream velocity peak in the open air is 120% of the train speed in open air but reduces by 30% when the train nose is halfway through the tunnel.
- Inside the tunnel the velocity in the upstream region is significantly increased compared to open air, forming approximately 25% of the nose peak.

## Funding

The author(s) disclosed receipt of the following financial support for the research, authorship, and/or publication of this article: The first author was supported by an EPSRC Scholarship from the School of Engineering of the University of Birmingham.

## References

1. Flynn D, Hemida H, Soper D, et al. Detached-eddy simulation of the slipstream of an operational freight train. *Journal of Wind Engineering and Industrial Aerodynamics* 2014; 132: 1-12.
2. Soper D, Baker C and Sterling M. An experimental investigation to assess the influence of container loading configuration on the effects of a crosswind on a container freight train. *Journal of Wind Engineering and Industrial Aerodynamics* 2015; 145: 304-317.
3. Baker C. A review of train aerodynamics Part 1: Fundamentals. *The Aeronautical Journal* 2014 b; 118.
4. Kikuchi K, Lida M and Fukuda T. Optimization of train nose shape for reducing micro-pressure wave radiated from tunnel exit. *Journal of Low Frequency Noise, Vibration and Active Control* 2011; 30: 1-19.
5. Yoon TS, Lee S, Hwang H, et al. Prediction and validation on the sonic boom by a high-speed train entering a tunnel. *Journal of Sound and vibration* 2001; 247: 195-211.
6. Baker CJ, Dalley SJ, Johnson T, et al. The slipstream and wake of a high-speed train. *Proceedings of the Institution of Mechanical Engineers, Part F: Journal of Rail and Rapid Transit* 2001; 215: 83-99.
7. CEN. Railway applications - Aerodynamics. Part 3: Aerodynamics in tunnels. BSI Standards Limited, 2003.
8. Ricco P, Barron A and Molteni P. Nature of pressure waves induced by a high-speed train travelling through a tunnel. *Journal of Wind Engineering and Industrial Aerodynamics* 2007; 95: 781-808.
9. Ko Y, Chen C, Hoe I, et al. Field measurements of aerodynamic pressures in tunnels induced by high speed trains. *Journal of Wind Engineering and Industrial Aerodynamics* 2012; 100: 19-29.
10. William-Louis M and Tournier C. A wave signature based method for the prediction of pressure transients in railway tunnels. *Journal of Wind Engineering and Industrial Aerodynamics* 2005; 93: 521-531.
11. CEN. EN 14067-5: 2006+A1: 2010 Railway Applications - Aerodynamics Part 5: Requirements and test procedures for aerodynamics in tunnels. CEN, 2010.
12. Baker C. A review of train aerodynamics, Part 2 - Applications. *The Aeronautical Journal* 2014 a; 118.
13. Vardy AE. Aerodynamic drag on trains in tunnels Part 1: Synthesis and definitions. *Proceedings of the Institution of Mechanical Engineers Part F Journal of Rail and Rapid Transit* 1996; 210: 29-38.
14. Vardy AE. Aerodynamic drag on trains in tunnels: Part 2: Prediction and validation. *Proceedings of the Institution of Mechanical Engineers Part F Journal of Rail and Rapid Transit* 1996; 210: 39-49.
15. Curie IG. *Fundamental Mechanics of Fluids*. Fourth Edition ed.: Taylor & Francis Inc, CRC Press Inc., 2012.
16. Singh NK and Sarkar S. DNS of a Laminar Separation Bubble. *International Journal of Mechanical and Mechatronics Engineering* 2011; 5.
17. Chang PK. Separation of flow. *Journal of The Franklin Institute* 1961; 272.

18. Bushnell DM and Moore KJ. Drag Reduction in Nature. *Annual Review of Fluid Mechanics* 1991; 23: 65-79.
19. Soper D. *The aerodynamics of a container freight train*. University of Birmingham, 2014.
20. Jahanmiri M. Laminar separation bubble: Its structure, dynamics and control. Goteborg, Sweden: Department of Applied Mechanics, Chalmers University of Technology, 2011.
21. Diwan, S. S. and Ramesh ON. Laminar separation bubbles: Dynamics and control. *Sadhana* 2007; 32: 103-109.
22. Kim J and Moin P. Application of a fractional-step method to incompressible Navier-Stokes equations. *Journal of Computational Physics* 1985; 59: 308-323.
23. Kiya M and Sasaki K. Free-stream turbulence effects on a separation bubble. *Journal of Wind Engineering and Industrial Aerodynamics* 1983; 14: 375-386.
24. Arakeri VH and Acosta AJ. Viscous effects in the inception of cavitation on axisymmetric bodies. *Journal of Fluids Engineering* 1973; 95: 519-527.
25. Samson A, Sarkar S and Anand K. Experimental investigation of a separation bubble on a flat plate with semi-circular leading edge for different Reynolds numbers. *9th International Conference on Heat Transfer, Fluid Mechanics and Thermodynamics*. Malta 2012.
26. Bokhortst E, Kat R, Elsinga GE, et al. Feather roughness reduces flow separation during low Reynolds number glides of swifts. *Journal of Experimental Biology* 2015; 218: 3179-3191.
27. Sajben M. Fluid mechanics of train-tunnel systems in unsteady motion. *AIAA* 1970; 9: 1538-1545.
28. Zhang L, Yang M, Liang X, et al. Oblique tunnel portal effects on train and tunnel aerodynamics based on moving model tests. *Journal of Wind Engineering and Industrial Aerodynamics* 2017; 167: 128-139.
29. Flynn D, Hemida H and Baker C. On the effect of crosswinds on the slipstream of a freight train and associated effects. *Journal of Wind Engineering and Industrial Aerodynamics* 2016; 156: 14-28.
30. Khayrullina A, Blocken B, Janssen W, et al. CFD simulation of train aerodynamics: Train-induced wind conditions at an underground railroad passenger platform. *Journal of Wind Engineering and Industrial Aerodynamics* 2015; 139: 100-110.
31. Huang Y, Hong TH and Kim CN. A numerical simulation of train induced unsteady airflow in a tunnel of Seoul subway. *Journal of Mechanical Science and Technology* 2012; 26: 785-792.
32. Araujo P and Rezende A. Comparison of turbulence models in the flow over a backward-facing step. *International Journal of Engineering Research & Science* 2017; 3.
33. Hemida H and Krajnovic S. LES study of the influence of the nose shape and yaw angles on flow structures around trains. *Journal of Wind Engineering and Industrial Aerodynamics* 2010; 98: 34-46.
34. Iliadis P, Soper D, Baker C, et al. Experimental investigation of the aerodynamics of a freight train passing through a tunnel using a moving model. *Proceedings of the Institution of Mechanical Engineers, Part F: Journal of Rail and Rapid Transit* 2018. DOI: 10.1177/0954409718811736.
35. Johnson T and Dalley S. 1/25 Scale Moving Model Tests for the TRANSAERO Project. In: Schulte-Werning B., Grégoire R., Malfatti A., Matschke G. (eds) TRANSAERO — A European Initiative on Transient Aerodynamics for Railway System Optimisation. *Notes on Numerical Fluid Mechanics and Multidisciplinary Design (NNFM)* 2002; 79: 123-135.
36. Ansys. CFX Modelling Guide. Release 16.2. SAS IP, Inc., 2015.
37. Liu Y, Hemida H and Liu Z. Large eddy simulation of the flow around a train passing a stationary freight wagon. *Proceedings of the Institution of Mechanical Engineers, Part F: Journal of Rail and Rapid Transit* 2014; 228: 535-545. DOI: 10.1177/0954409713488096.
38. TSI. Commission Regulation (EU) No 1302/2014 of 18 November 2014 concerning a technical specification for interoperability relating to the 'rolling stock - locomotives and passenger rolling stock' subsystem of the rail system in the European Union. In: Commission E, (ed.). Official Journal of the European Union, 2014.

39. Moussaed C, Salvetti M, Wornom S, et al. Simulation of the flow past a circular cylinder in the supercritical regime by blending RANS and variational-multiscale LES models. *Journal of Fluids and Structures* 2014; 47: 114-123.
40. Temple J and Johnson T. Effective Management of Risk from Slipstream Effects at Tracksides and Platforms. *Technical Report: A Report Produced for Rail Safety and Standards Board*. 2008.
41. Sterling M, Baker C, Jordan SC, et al. A study of the slipstream of high speed passenger trains and freight trains. *Proceedings of the Institution of Mechanical Engineers, Part F: Journal of Rail and Rapid Transit* 2008; 222: 177-193.
42. Sturm H, Dumstorff G, Busche P, et al. Boundary layer separation and reattachment detection on airfoils by thermal flow sensors. *Sensors* 2012; 12: 14292-14306.
43. Jovic S. An experimental study of a separated/reattached flow behind a backward-facing step. *NASA Technical Memorandum 110384*. Elort Institute, Ames Research Center, Moffet Field, California: NASA, 1996.
44. Driver DM, Seegmiller HL and Marvin JG. Time-dependent behavior of a reattaching shear layer. *AIAA Journal* 1987; 25: 914-919.
45. Neumann J. On time-dependent behaviour of controlled turbulent flow with separation and reattachment. In: *PAMM Proceedings in Applied Mathematics and Mechanics 3* 2003, pp.44-47.
46. Soper D, Baker C and Sterling M. Experimental investigation of the slipstream development around a container freight train using a moving model facility. *Journal of Wind Engineering and Industrial Aerodynamics* 2014; 135: 105-117.
47. Baker C. The flow around high speed trains. *Journal of Wind Engineering and Industrial Aerodynamics* 2010; 98: 277-298.

## Appendix

### Nomenclature

A	Cross-sectional area of the tunnel (m <sup>2</sup> )
c	Speed of sound (m/s)
H	maximum height of separation bubble vortex
h	Locomotive height (m)
I	Turbulence Intensity (%)
k	Turbulence Kinetic Energy (J/kg)
L	Locomotive length (m)
p	Pressure (Pa)
R	Reynolds-Averaged Navier-Stokes equations
T	Temperature (K)
TSI	Technical Specifications for Interoperability
t	Time (s)
U <sub>x</sub>	Longitudinal component of flow velocity (m/s)
V	Train speed (m/s)
v	Volume (m <sup>3</sup> )
x	Distance from the origin of the longitudinal axis (m)
y	Distance from the origin of the vertical axis (m)
z	Distance from the origin of the lateral axis (m)
μ	Dynamic viscosity (Pa·s)
τ	Wall shear stress (Pa)
ω	Specific Dissipation rate (s <sup>-1</sup> )